XMM-Newton CCF Release Note

XMM-CCF-REL-348

Modification of the XRT PSF Parameters

M.J.S. Smith, D. Lumb, R. Saxton and N. Schartel

August 24, 2017

1 CCF Components

Name of CCF	VALDATE	EVALDATE	Blocks Changed
XRT1_XPSF_0016.CCF	2000-01-13T00:00:00		ELLBETA_PARAMS
XRT2_XPSF_0016.CCF	2000-01-13T00:00:00		ELLBETA_PARAMS
XRT3_XPSF_0018.CCF	2000-01-13T00:00:00		ELLBETA_PARAMS

2 Changes

This release consists of two changes to the PSF modelling:

- a refinement of the parameters describing the PSF shape;
- a change to the PSF normalisation radius.

The former only affects EPIC spectral analysis of sources located within $3'$ of the telescope boresight, whereas the latter affects sources throughout the complete EPIC field-of-view.

2.1 Refinement of PSF Model Parameters

Several studies of EPIC spectra of non-piled-up point sources have shown systematic dependencies on the size of the extraction region. In particular, PN spectra extracted from data obtained from the PSF core have shown significant differences with respect to those from the PSF wings. These

discrepancies are evident above ~ 4.5 keV, and are characterised by an increasing flux deficit towards higher energies and further into the PSF wings of up to 30% above ~ 8.0 keV at radii of $\sim 60''$. Analyses performed on MOS spectra indicated similar discrepancies, although to lesser extent.

While affecting all point sources, this issue becomes especially important in the spectral analysis of piled-up sources, where the need to excise the piled-up data from the spectra requires the use of annular extraction regions. In these cases, the larger relative contribution of the PSF wings will result in a more pronounced spectral distortion.

The origin of the issue lies in current imperfections of the energy dependent PSF modelling. This release aims at a correction through a refinement of the parameters which model the PSF. A detailed description of the PSF parameterisation is given in Read et al. (2010).

To this end, relevant PSF parameters were iteratively optimised in order to minimise spectral residuals of a set of nested annular extractions with respect to the best-fit model to the encompassing circular extracted spectrum. Per telescope, the optimisation was performed simultaneously on a sample of non-piled-up point sources, and consisted of minimising the total χ^2 across all annuli and sources.

In order to reduce the parameter space, the optimisation was limited to the King function core radius (r_0) and slope index (α), as these are the dominant parameters affecting the PN telescope PSF close to the boresight. In terms of energy dependence, only parameters describing the PSF above 2.0 keV were varied, with the additional constraint of tying the highest energy parameters at 15.00 keV to those at 10.25 keV.

Moreover, the parameters were chosen to be optimised for sources located at the respective instrument nominal aim points, which lie at off-axis angles of $\sim 0.17'$ for MOS1 and $\sim 1.12'$ for MOS2 and PN. To this end, for the MOS2 and PN telescopes (XRT2 and XRT3, respectively) an additional off-axis tabulation at $1.12'$ was introduced in the parameterisation; the on-axis values were tied to these. For the MOS1 telescope (XRT1), where the nominal aim point lies much closer to the telescope axis, it was sufficient to optimise the on-axis values. For all three telescopes, the parameters describing the PSF at larger off-axis angles remain unchanged, and hence the modifications described in this section affect only the central $3.0'$ of the fields-of-view.

The data sample was selected on the basis of bright non-piled up point sources observed close to the instrument aim points (see Table 1). The most suitable spectra for the purpose are highly absorbed, allowing a proportionally larger number of counts towards higher energies without running into pile-up. Owing to the dearth of highly absorbed sources observed in Full Frame Mode it was necessary to include several PN Small Window Mode observations of such sources in the sample (these observations could not be used for MOS due to pile-up). Data were further selected on low instrumental and flaring backgrounds, and PN spectra were corrected for out-of-time events.

The respective radii of the nested annuli were chosen in order to obtain similar source counts for each, although the innermost radius was restricted to be substantially larger than the physical pixel size. The outermost radius was limited to $60''$ in order to maintain a sufficient signal-to-noise ratio (for Small Window Mode observations the outer radius was limited to $40''$ in order to avoid additional uncertainties due to the encircled energy correction beyond the read-out window).

Table 1: Target sample used in the PSF parameter optimisation, with respective instrumental set-ups where applicable.

Target	Rev	ObsID	PN		MOS1		MOS2	
			Mode	Filter	Mode	Filter	Mode	Filter
MS0205.7+3509	0217	0084140101	FF	Thin	FF	Medium	FF	Medium
Holmberg IX	0428	0112521001	FF	Thin	FF	Thin	FF	Thin
Markarian 6	0619	0144230101	FF	Medium	FF	Medium		
PKS B1334-127	0576	0147670201	FF	Thin	FF	Thin	FF	Thin
RX J0228-40	0915	0200480101	FF	Thin	FF	Thin	FF	Thin
LBQS 1228+1116	1103	0306630201	FF	Thin	FF	Medium	FF	Medium
NGC 5506	1661	0554170101	SW	Thin				
NGC 5506	1581	0554170201	SW	Thin				
RBS 1055	1558	0555020201	FF	Thin	FF	Thin	FF	Thin
MCG-5-23-16	2480	0727960101	SW	Thin				
MCG-5-23-16	2481	0727960201	SW	Thin				

2.2 Change in PSF Normalisation Radius

The SAS implementation of the telescope response combines a normalised PSF with telescope effective area data. The PSF normalisation entails integrating the model up to the normalisation radius, which is defined by the `NORM_AT` header keyword value contained in the `ELLBETA_PARAMS` extension of the `XRTn_XPSF` CCFs. The telescope effective area data are contained in the `XRTn_XAREAEF` CCFs.

The SciSim ray-trace simulator was used to obtain simulated mirror effective areas as a function of the PSF normalisation radius. Comparison of these results with mirror effective area calibration data show that the currently implemented normalisation radius of $5.0'$ yields overestimates of the telescope effective area by $\sim 1.5\%$ at 1.5 keV and $\sim 6\%$ at 8 keV.

In this release the normalisation radius has been increased to $15.0'$ in order to obtain consistent results. This change will affect response files for spectra extracted from the full fields-of-view of the three EPIC cameras.

3 Scientific Impact and Estimated Quality

3.1 PSF Parameters and EEF

A comparison of relevant current PSF model parameters and those resulting from the aforementioned optimisation are shown in Fig. 1. The values shown pertain to the nominal aim point off-axis angles and are either directly tabulated in the CCF (XRT2 and XRT3) or obtained through interpolation (XRT1, interpolating between the $0.0'$ and $3.0'$ tabulated values). The changes are similar for the three telescopes, showing a slight drop in core radius at high energies and a flattening of the slope. The changes in the MOS telescope parameters are within 5%, those of the PN are larger, up to 7% in core radius, and 12% in slope.

The resulting changes in terms of PSF encircled energy function (EEF) at several energies are shown in Fig. 2. The main effect consists of a narrowing of the PN PSF in terms of energy width above 6 keV. The changes to both MOS EEFs is less significant, but both show a slight widening around $6 - 8$ keV. Overall, the new PSF parameters result in a more similar EEF across the three telescopes.

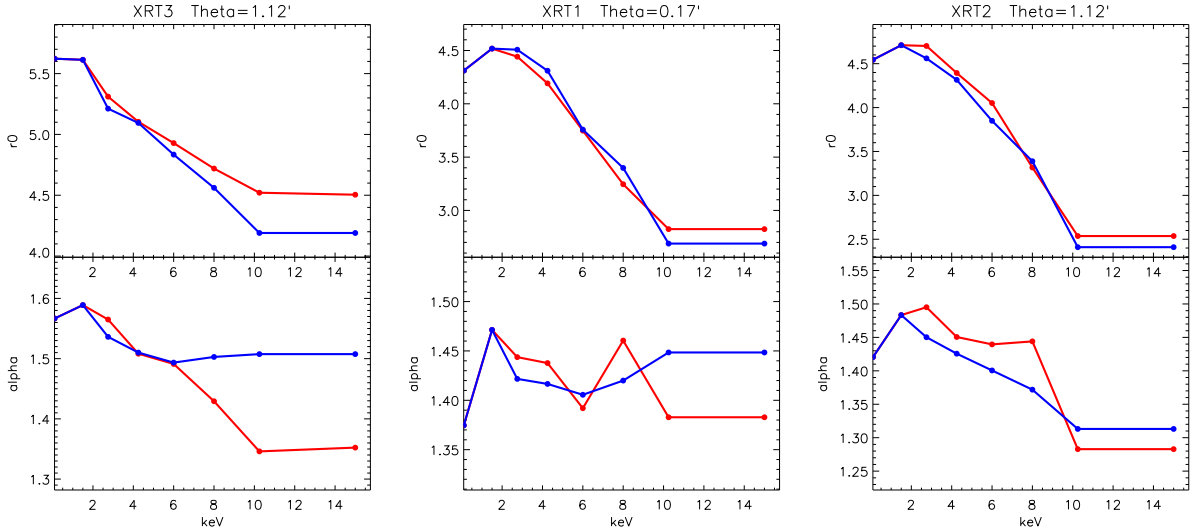

Figure 1: Comparison of PSF model parameters as function of energy at the respective nominal aim points of the three telescopes: from left to right: PN (XRT3), MOS1 (XRT1) and MOS2 (XRT2). Top and bottom panels show the King function core radius (r_0) and slope (α), respectively. The currently implemented parameters and those resulting from the optimisation are shown in red and blue, respectively.

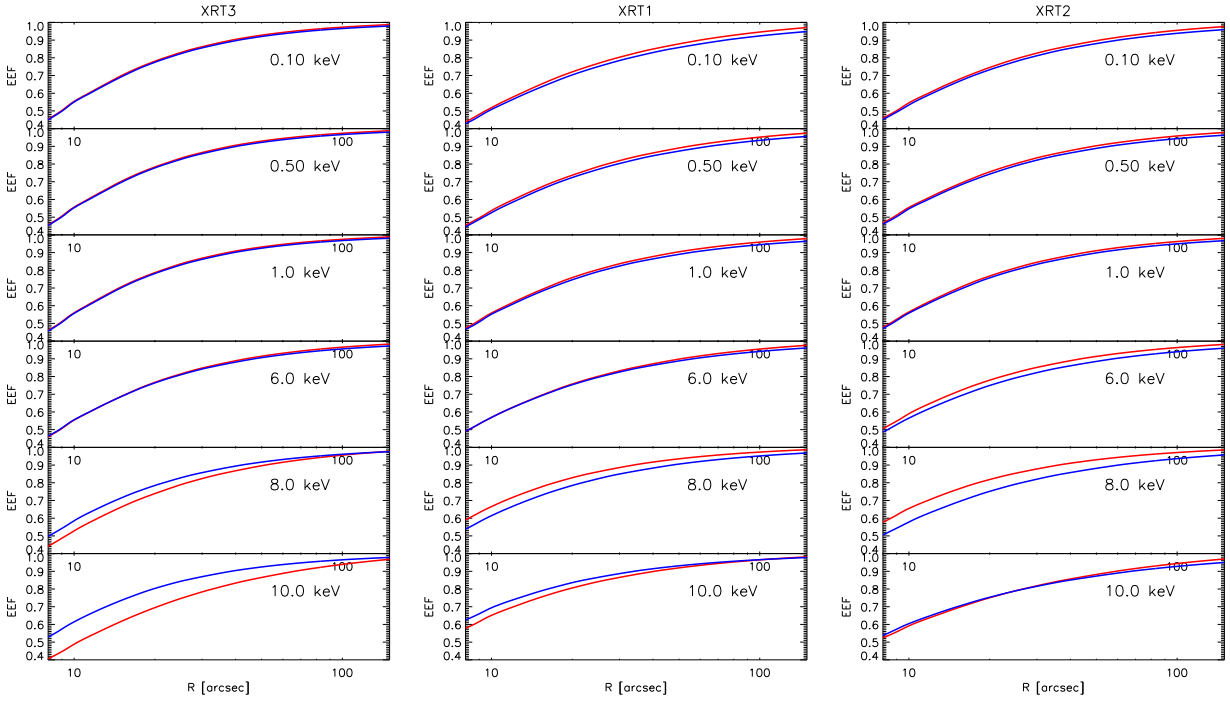

Figure 2: Comparison of the EEF for the respective nominal aim points at different energies. From left to right: PN (XRT3), MOS1 (XRT1) and MOS2 (XRT2). Current and new PSFs are shown in red and blue, respectively.

3.2 Spectral Impact

3.2.1 Optimisation Sample

Although the optimisation will by construction result in an overall improvement in fit statistic, this is not necessarily the case for all spectral fits per annular region. The results for the latter are shown in Fig. 3, illustrating the change in statistic per annular bin in terms of the reduced χ^2 distribution. The major changes are seen for PN, where for all annuli the reduced χ^2 distribution is reduced post-optimisation, especially in the core and in the $20'' - 40''$ range. The changes for both MOSs are less significant, but in general tend to narrower distributions, and in no case is there significant worsening.

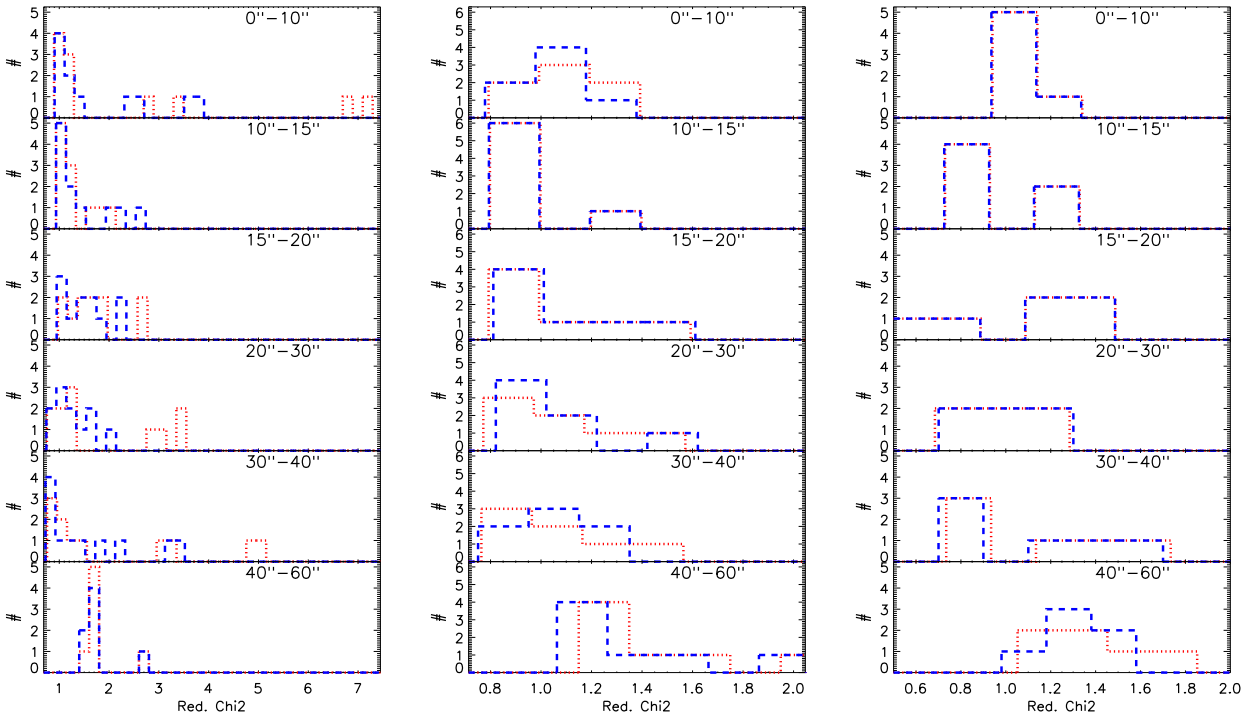

Figure 3: Comparison of fit statistic in terms of reduced χ^2 distribution per annular bin. From left to right: PN, MOS1 and MOS2. The situation with the current PSF parameters and with the optimised parameters in this release is shown in red and blue, respectively.

Several representative spectral results of individual sources are shown in Figs. 6 to 9. Per annular region the residuals with respect to the best fit model to the encompassing circular extracted spectrum are shown, comparing results of the current calibration with those obtained with this release. The respective reduced χ^2 values are labelled.

Observation 0112521001 (Holmberg IX, see Fig. 6) shows moderate improvements in terms of reduced residuals for MOS1 and MOS2, especially for larger annular radii. PN data show no significant changes. Observation 0144230101 (Markarian 6, see Fig. 7) shows more significant improvements, especially for the PSF core and annular radii larger than $20''$ for PN and $30''$ for MOS1.

For observations 0554170101 (NGC 5506, Fig. 8) and 0727960101 (MCG-5-23-16, Fig. 9) there is only suitable data for PN. These highly absorbed spectra yield significant data at high energies. Apart from the $10''-15''$ annulus, the improvements obtained are marked, with significant reduction above ~ 4.5 keV of the flux excess in the PSF core and the deficits in the annuli (up to 30% reduction in the largest annuli).

In general, for the sample of sources used in the optimisation this release yields greater consistency of residuals across the PSF, their shape being very much flattened up to $60''$ extractions. However, it should be noted that discrepancies in terms of normalisation of the order of 10-20% in the PSF wings remain present with this new release.

There is some impact of the changes to the PSF on the total spectrum (i.e. that extracted with a circular region of sufficient radius). Below ~ 3 keV the effect is negligible. However, in terms of high energy (~ 5 keV) power law slope the new release yields on average a higher photon index for PN and a lower photon index for the MOSs; the absolute size of the change is ~ 0.07.

3.2.2 Blazar Sample

A validation of the new PSFs was performed on an independent set of EPIC data consisting of a sample of 23 bright blazars, all observed in Small Window Mode. Due to the high count rates the observations are subject to pile-up, and the spectra are extracted from annular regions (with typical inner and outer radii of $\sim 15''$ and $\sim 40''$, respectively). For each observation, spectra were obtained from strictly simultaneous good-time intervals across all instruments. Per instrument, the spectra were fit yielding fluxes in several bands; these were then normalised to those of the PN. Per band the mean flux ratios across the sample were determined. Fig. 4 compares the results obtained with the current PSF and this release. The large flux excess of the MOSs versus PN above ~ 3.5 keV has been significantly reduced, down from $\sim 25\%$ to $\sim 15\%$ in the highest band. The residual discrepancies between MOSs and PN are similar in shape and magnitude to those seen for source spectra obtained from standard circular extractions (see e.g. Read et al. 2014), and are likely not PSF related. Note the RGS fluxes are not impacted by the PSF changes.

3.2.3 Pipeline Products

Over 130 recent observations were processed through the XMM-Newton Pipeline Processing System (PPS) using the current and new CCFs in order to determine the impact on broad band count rates in the detected sources. The ~ 8700 cross-matched sources were divided into two samples, namely those within and beyond $3'$ off-axis angle. Results of the latter are only affected by the change in PSF normalisation radius, whereas those of the former are additionally affected by the modified PSF parameters.[1]

The results are summarised in Fig. 5, which shows relative count rate differences per PPS spectral band. For the source sample within $3'$ off-axis angle there are no significant effects below 2.0 keV.

[1] In terms of source detection, the change in PSF parameters may have some impact beyond $3'$ off-axis angle due to background fits being affected to some extent.

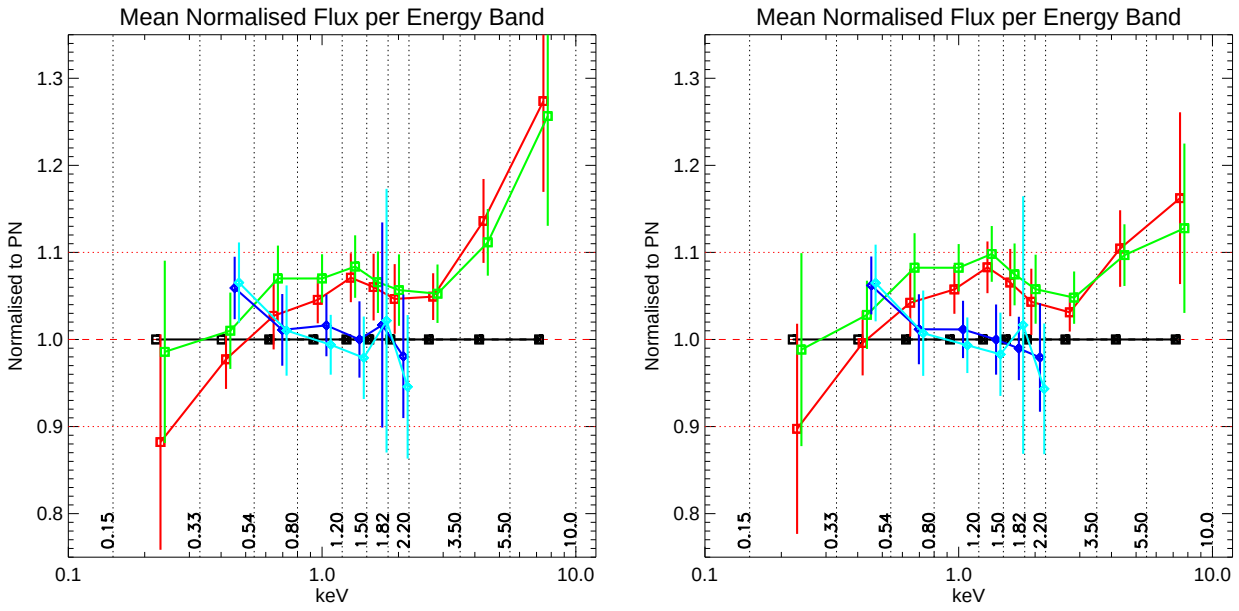

Figure 4: Relative fluxes per energy band of a sample of bright blazar observations. Fluxes shown are the instrumental sample means normalised to those of the PN. Colour coding: PN (black), MOS1 (red), MOS2 (green), RGS1 (blue) and RGS2 (magenta). Left panel shows results obtained with the current calibration, right panel those obtained with the current release.

For the MOSs the new CCFs yield a slight increase in relative count rates in the two highest bands, peaking at $\sim 5\%$ for MOS1 and $5-10\%$ for MOS2. For PN, the highest band shows a $5-10\%$ drop in count rates. These results are qualitatively consistent with the spectral change in terms of powerlaw slope as described in Section 3.2.1. For the source sample beyond the $3'$ off-axis angle cut the MOSs show a slightly larger increase in high energy count rates, up to $\sim 10\%$. Likewise, for PN the high energy count rate deficit has turned over into a $\sim 5\%$ excess. These results may be explained by the change in normalisation radius, which impacts most towards energies where the PSF shape is broadest. Thus the correction to the currently overestimated effective area is strongest at high energies.

3.3 Radial Profiles

The impact of the changes in PSF parameters on radial profiles was investigated for the optimisation source sample using the SAS task `eradial`. This task allows the radial profile to be compared to a linear fit of the normalised PSF. For Full Frame Mode data the comparison is performed up to a $180''$ radius. For Small Window Mode the comparison has been truncated at a radius of $40''$ in order to remain within the read-out window. Representative results of both modes are described below.

Observation 0084140101 (MS0205.7+3509, see Fig. 10) shows no significant changes in the PSF fits to the radial profiles. The overall fit is good showing the PSF remains well constrained up to $180''$ radius.

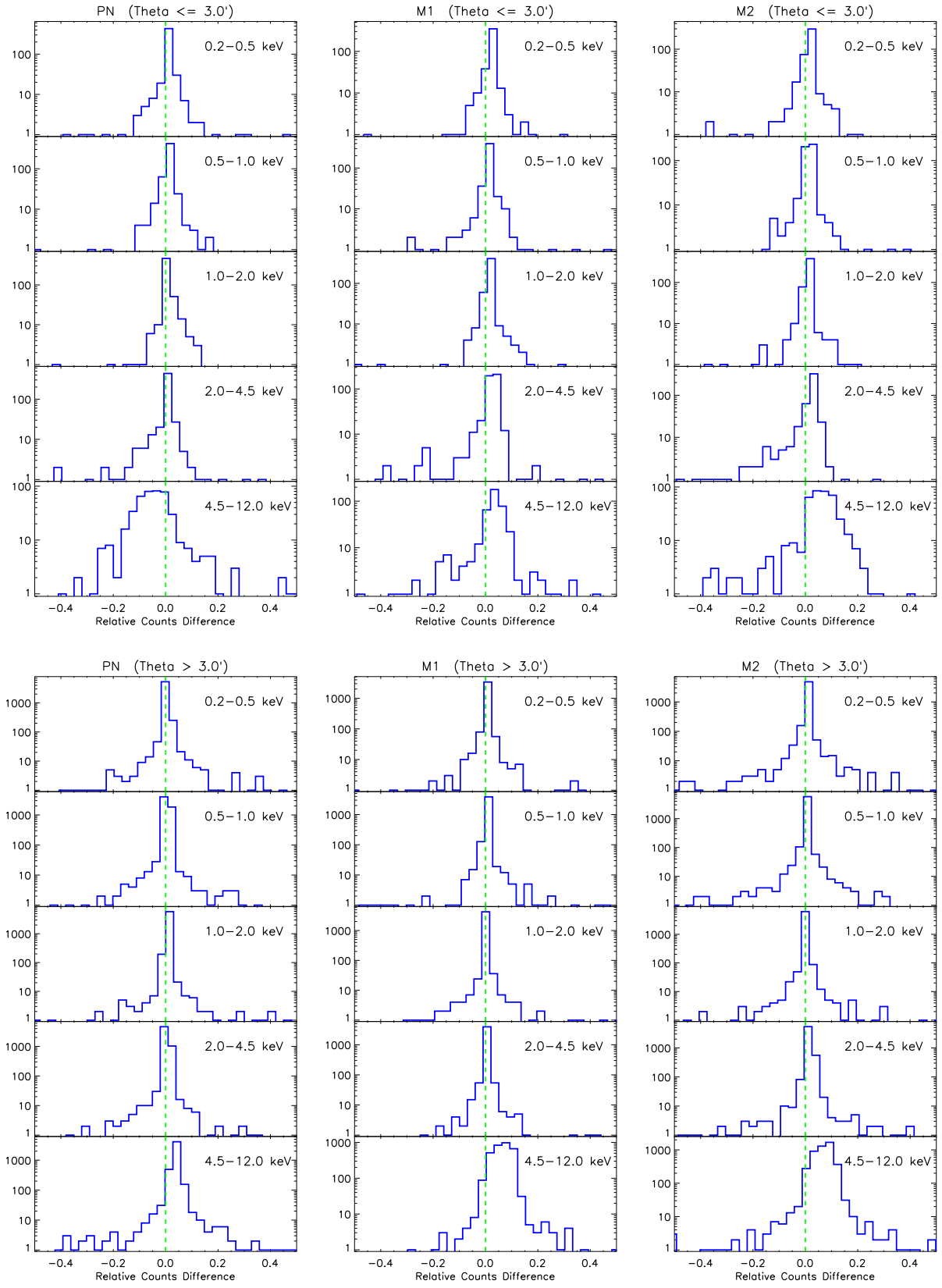

Figure 5: Relative count rate difference distribution per energy band of sources detected in a set of PPS processed observations. The count rate difference is defined as *(new - old)/old* where *old* refers to rates obtained with the current calibration and *new* refers to those obtained using this release. From left to right: PN, MOS1 and MOS2. Top and bottom panels include only sources detected within and beyond 3′ of the boresight, respectively.

Observation 0554170101 (NGC 5506, Fig. 11), a Small Window Mode observation with significant high energy counts, shows a slight worsening of the fit at medium energies, but a marked improvement in the highest energy band. The increasing data-to-model deviations above 30″ have been significantly reduced, from $\sim 40\%$ down to $\sim 10\%$.

In general, across the sample the radial profile fits for the MOSs do not significantly change. For PN the high energy PSF gives more consistent results towards higher radii.

3.4 Impact on Source Detection

The impact of the CCF release on large scale source detection was investigated using the PPS processing sample as described in Section 3.2.3. For the full field of view, out of 8724 detected sources, the number of sources which were not cross-matched is 55 (26 point sources, and 29 extended sources), i.e. 0.7%. For the central 3′ area the numbers are 24 mismatches (12 point sources, 12 extended sources) out of a total of 635 detections. An investigation of the latter sample shows that the mismatches pertain to marginal detections with likelihoods < 15.

4 Test Procedures

Verification of functionality with SAS 16.0: `calview`, `cifbuild`, `arfgen`.

5 Expected Updates

There is scope for further refinement of PSF parameters. This release affects only the near on-axis PSF, and even then only a limited subset of parameters has been subject to modification. E.g., the parameters which describe the gauss component of the PSF model remain unchanged; although only $< 5\%$ of the EEF would be affected, inclusion these parameters in the analysis may nevertheless allow a reduction of the core-to-wings normalisation discrepancy. Moreover, the energy dependence of the model parameters at larger off-axis angles is currently under investigation in order to ensure the PSF is properly constrained across the field-of-view.

6 References

Read, A.M., et al., 2010, XMM-CCF-REL-263
(`http://xmm2.esac.esa.int/docs/documents/CAL-SRN-0263-1-3.ps.gz`)

Read, A.M., et al., 2014, A&A, 564, 75

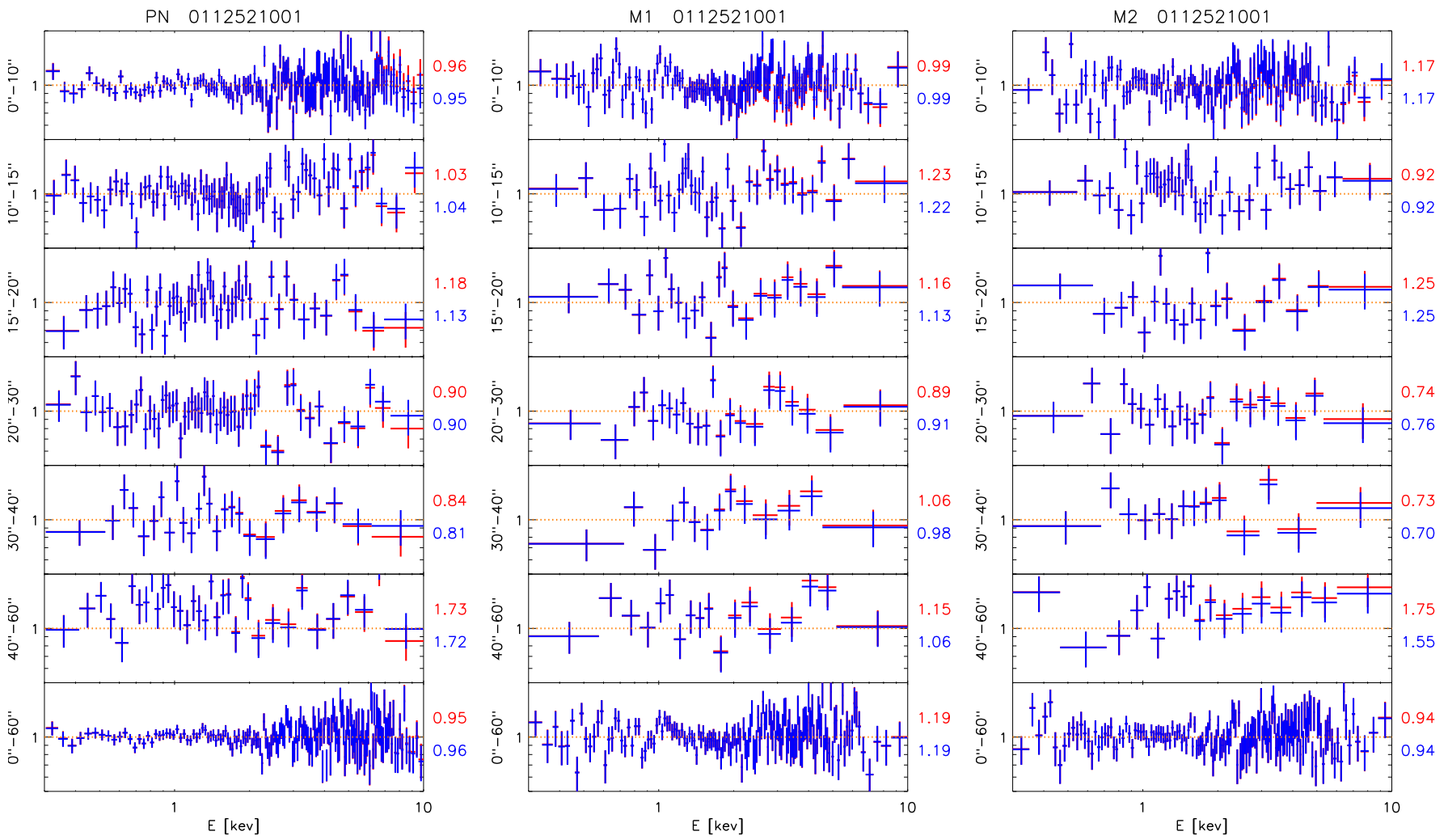

Figure 6: Residuals of spectra extracted from annular regions with respect to the best fit model to the encompassing circular extraction. Results obtained with the current calibration are shown in red, and those with this release in blue. The respective reduced χ^2 values are labelled. From left to right: PN, MOS1 and MOS2. Observation 0112521001 (Holmberg IX).

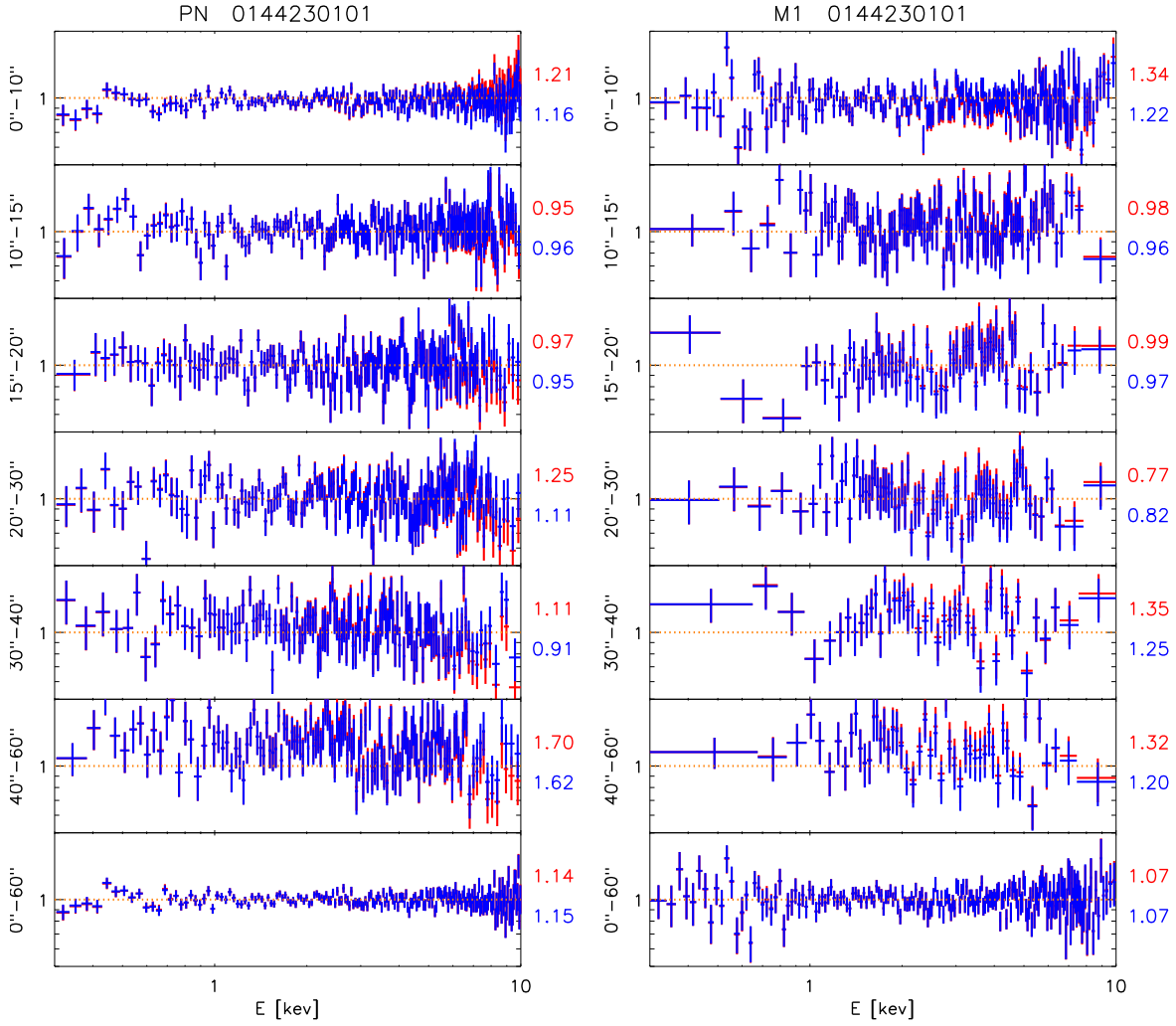

Figure 7: As Fig. 6 but for observation 0144230101 (Markarian 6); no MOS2 data available.

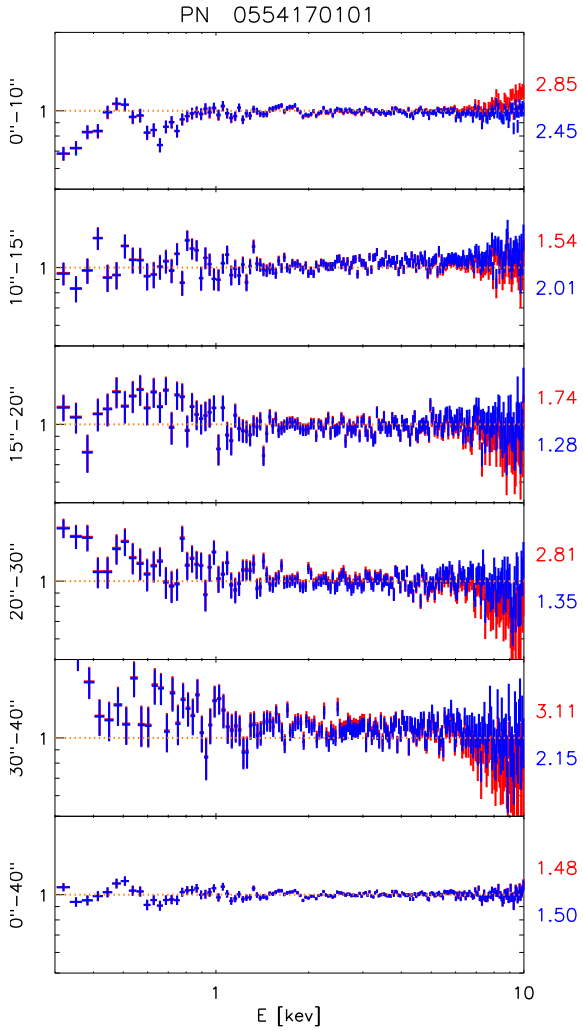

Figure 8: As Fig. 6 but for observation 0554170101 (NGC 5506); no MOS1 or MOS2 data available.

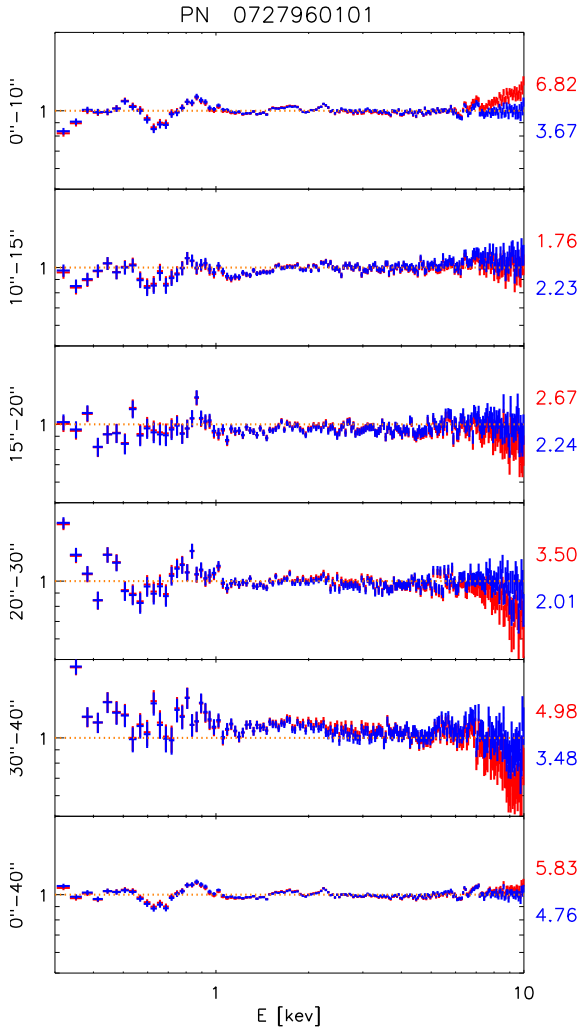

Figure 9: As Fig. 6 but for observation 0727960101 (MCG-5-23-16); no MOS1 or MOS2 data available.

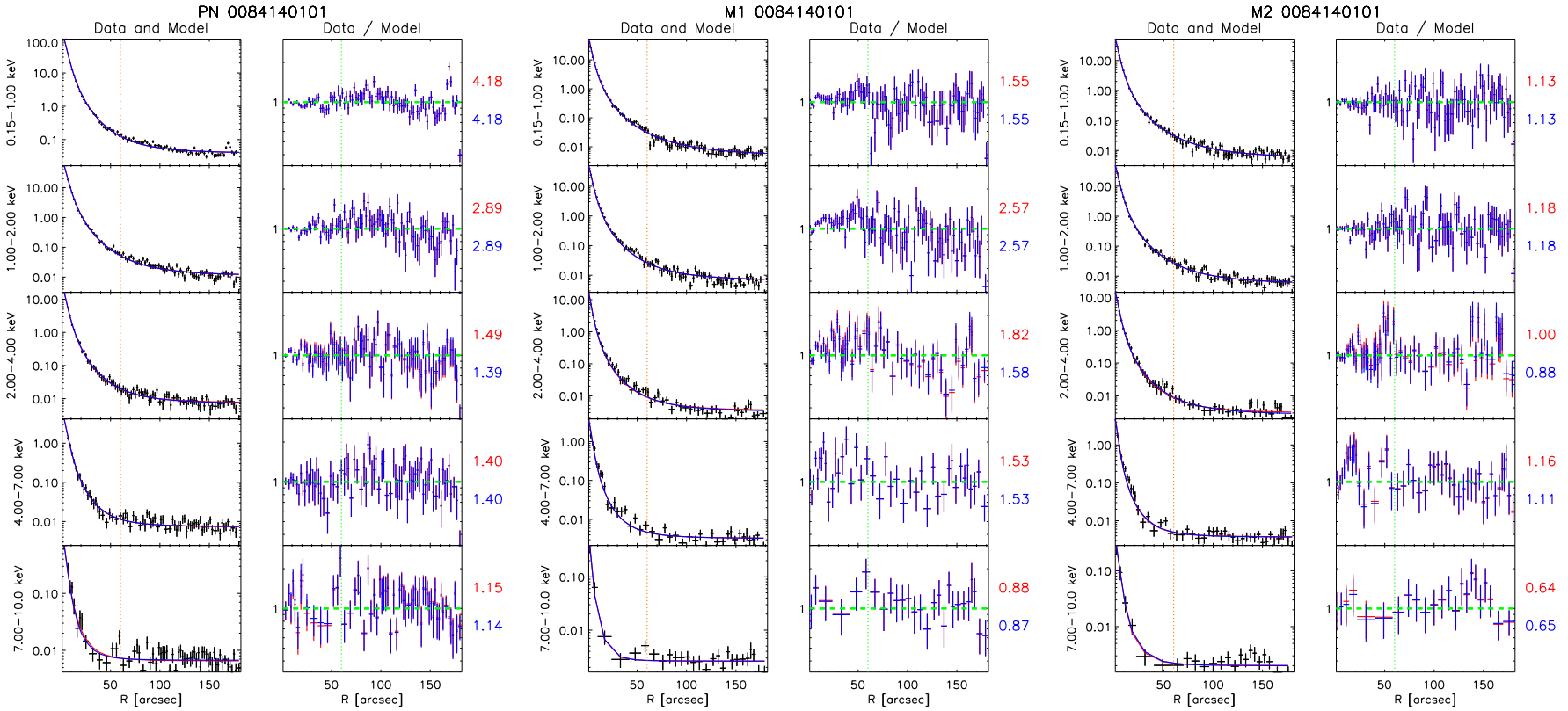

Figure 10: Radial profiles (left column) and residuals to the best linear fit of the PSF (right column) for several energy bands, per instrument (from left to right: PN, MOS1 and MOS2). The residuals of the current calibration are shown in red, and those of this release in blue. The best fit reduced χ^2 values are indicated. Data were rebinned to a signal-to-noise ratio of 3. Observation 0084140101 (MS0205.7+3509).

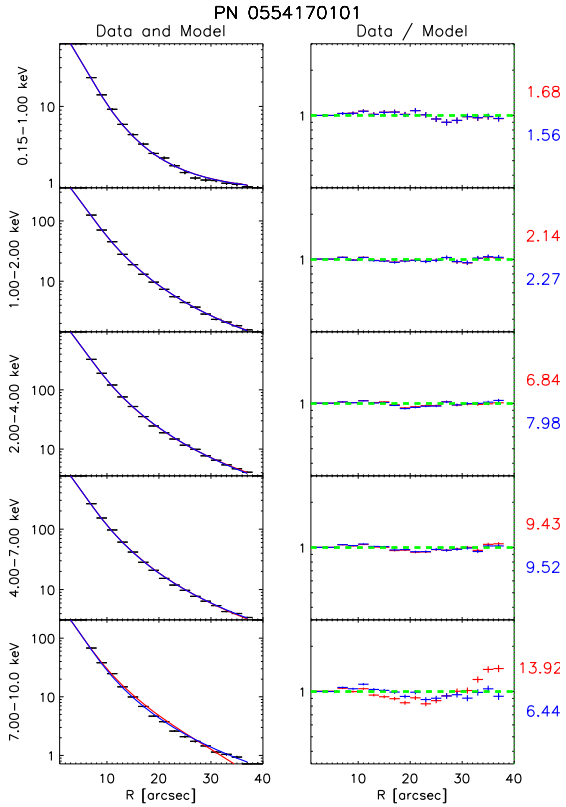

Figure 11: As Fig. 10 but for observation 0554170101 (NGC 5506); no MOS1 or MOS2 data available.